PERGAMON International Journal of Multiphase Flow 24 (1998) 1265–1294

International Journal of Multiphase Flow

Monofiber optical probes for gas detection and gas velocity measurements: conical probes

A. Cartellier *, E. Barrau

LEGI, Laboratoire des Écoulements Géophysiques et Industriels, UMR 5519, UJF-CNRS-INPG, BP 53, F-38041, Grenoble Cedex 9, France

Received 28 November 1996; received in revised form 11 March 1998

Abstract

Optical probes are a very common tool for the investigation of gas–liquid flow dynamics. A single sensitive tip gives access to the phase indicator function, while using two tips some distance apart provides estimates of the gas velocity. Recently, it has been shown that the gas velocity could also be inferred from a monofiber probe provided that its latency length is known. To improve the capabilities of this new technique, an optimisation of the probe geometry, based on optical simulations and controlled piercing experiments, has been undertaken. In this first paper, conical probes (1C) produced using a new manufacturing technique are considered. Although they are effective for simultaneous gas velocity measurements, their actual response is sensitive to small geometrical defects occurring at their tips. Therefore, calibrations on well controlled interfaces appear necessary both to check the presence of pre-signals responsible for incorrect phase detections, and to establish a significant rise-time/velocity correlation.

Keywords: Optical probe; Interface detection; Gas velocity; Interface piercing; Drainage; Bubble size distribution; Interfacial area density; Gas–liquid (flow)

1. Introduction

Intrusive phase detection sensors, most often based on optical or impedance phenomena, are of great interest for the whole class of fluid–fluid two-phase flows; indeed they provide the phase indicator functions, from which local concentrations and flow regimes can be inferred. Moreover, double probes give an estimate of the dispersed-phase velocity. With this

* Corresponding author.

0301-9322/98/$19.00
PII: S0301-9322(98)00032-9

knowledge, it is possible, under some conditions, to obtain the mean interfacial area density, the size distribution of inclusions and their total flux through a unit cross-sectional area (Cartellier and Achard, 1991). This information, which is of primary importance in describing and modelling two-phase flows, is at hand with sensors which are relatively simple in their operating principle, and easy to use. These characteristics explain the success of intrusive phase detection techniques in research as well as in industry, where most applications have dealt with gas–liquid flows. However, many problems concerning these instruments remain to be solved.

Apart from the somewhat large-scale alteration of the phase distribution resulting from the mere presence of the probe and its support in the flow, one crucial and still acute difficulty is linked with the unavoidable signal shaping sequence which transforms the available raw signal into an experimental gas phase indicator function X_{Gm} as close as possible to the actual one X_{G}. This question, to which an original contribution has been brought recently by Zun et al. (1995), cannot be fully disconnected from the design of the sensitive tips.

First, the tip geometry influences the signal dynamics as shown, for example, by Abuaf et al. (1978), and Frijlink (1987) for optical probes, and by Pinguet (1994) for impedance probes. Since discriminating between phases is hardly achievable within the noise amplitude, it is especially important to ensure a high signal to noise ratio (SNR) in order to detect weak pulses corresponding either to tiny bubbles or to small chords cut through larger inclusions. Such detections are crucial for concentration measurements, and are also needed for reconstructing accurate size distributions.

Second, the hydrodynamics of piercing plays a fundamental role since it controls the duration of signal transitions, and is responsible for deviations from the true phase indicator function (Cartellier and Achard, 1991). These phenomena strongly depend on the probe geometry as shown by Cartellier (1990) for optical probes in gas–liquid flows, and by Pinguet (1994) for impedance probes in fluid–fluid suspensions. Let us briefly summarise the phenomena occurring in gas–liquid flows. For liquid–gas transitions, the liquid inertia induces a surge of the interface before the liquid film breaks. Then the probe tip dries, a process slowed by wettability effects and by the drainage of the liquid film left on the probe. For the transitions from gas to liquid, the surge effect is much less pronounced due to the weaker gas inertia, and to capillary effects which often accelerate the wetting. Therefore, liquid-to-liquid transitions are usually much longer than gas-to-liquid ones. The analysis of such transitions across well-controlled interfaces has shown that their duration T_{u} is inversely proportional to the geometrical interface displacement velocity V_{i} when the probe is normal to the interface (this proportionality holds above a critical velocity V_{c} typically about 0.1 m/s). The signal transient can be thus crudely interpreted as the translation of an idealised plane interface along a characteristic distance L, the so-called latency length. L represents the overall spatial resolution of the sensor working as an interface detector, and is the result of the probe response to the instantaneous interface position and shape. For these reasons, this concept has been proposed as a basis for an objective comparison between probes regardless of the detection technique involved (Cartellier, 1990).

Another interest in the latency length relates to its connection with measurement error. Indeed, if the probe response is assumed to be a monotonic function of the interface position (a parameter which could be characterised by the three-phase line location for example), then L (respectively, T_{u}) provides an estimate of the interface deformation (respectively, the delay of

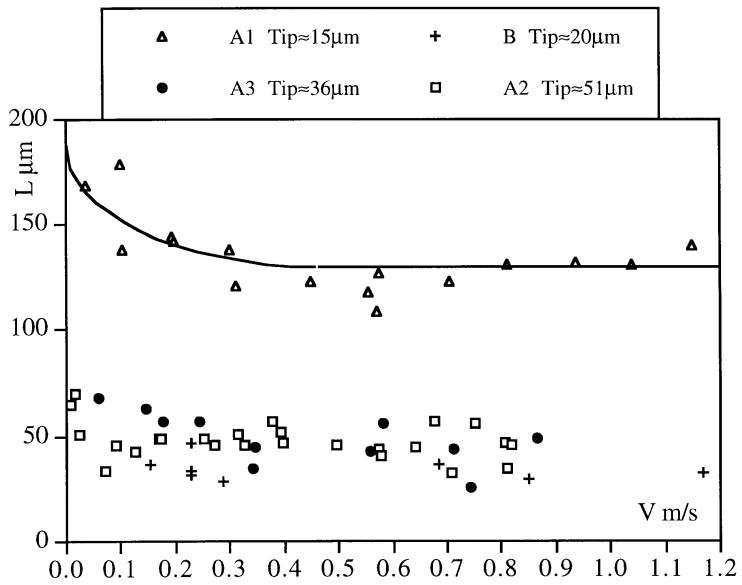

Fig. 1. Latency lengths for some stretched probes: A and B denote two manufacturers (the threshold levels are 10%–90% for A1, A2 and B, and 10%–80% for A3).

detection) between the position (respectively, the date of arrival) of the undisturbed interface (i.e. the interface which would exist in the absence of the intrusive sensor) and that of the deformed interface (which is the raw information available to the user). Thus, L (or T_u) controls the accuracy of the experimental phase indicator function. The discrepancy between X_{Gm} and X_G decreases with L, not only because detected interface positions become closer to undisturbed interface locations, but also because smaller chords can be better perceived due to a quick drying process, and also because steeper transitions are more easily and accurately identified by the signal processing. The reduction of L is then a clear objective in optimising phase detection. This aim is related to the on-going efforts devoted to manufacturing the smallest tips compatible with an acceptable SNR. For example, resistivity probes as thin as 11 μm are used by Zun et al. (1995). Monofiber optical probes, now usually obtained by melting and stretching silica fibers (such as 50/125 μm or 100/140 μm fibers), typically have a tip about 15–20 μm, and tips as small as 3 μm have been obtained by Gouirand (1990). However, the latency length, which can be seen as a measure of the sensitivity length of the probe, cannot be generally inferred from the tip size or length. This is clearly demonstrated for stretched monofiber optical probes in Fig. 1, where the sizes indicated are the hemispherical-tip diameters. For probe A1, whose shape is close to that of a bobbin, the loss of light extends over more than 100 μm, while probes A2 and A3, which are more conical and have larger tips, have shorter sensitivity lengths. This apparently contradictory observation is related to a better guidance of the light in the latter cases, resulting in the more direct polar distribution of light intensity emitted by the probe tip (see Fig. 3 in Cartellier 1992, where probes A1, A2 and A3 are referred as 1, 2, 3, respectively). Hence, the probe response not only depends on the fiber profile, but also on the distribution of the cladding thickness. These parameters which vary with stretching and heating conditions, are difficult to control. For these reasons, the

connection between the probe geometry and latency length is far from straightforward. Yet is should be mentioned that by carefully heating the tip after rupture of the fiber, capillary forces shape the extremity into a hemisphere. This technique, well known in biology, seems to be very dependent on the skill of the operator. Recently, Cubizolles (1996) has practised this manufacturing process and claims that good reproducibility of probe tips can be ensured. For the stretched probes obtained under these conditions, it seems that L has the magnitude of the tip size: this is exemplified by probe B in Fig. 1. However, a more detailed study of the connection between these shapes and the probe response is required before a definite conclusion can be drawn.

Aside from the search for very thin probes, another kind of optimisation could be of interest. Indeed, for a given probe, the knowledge of L allows determination of the interface displacement velocities from measurement of signal rise time T_u. This new technique has been proposed by Cartellier (1990), and its feasibility in real two-phase flows has already been demonstrated for a stretched optical monofiber (Cartellier, 1992) and for various impedance probes (Pinguet, 1994). It is worth mentioning that correlations for T_u in the form L/V have been previously identified by Werther and Molerus (1973) for resistivity probes and by Abuaf et al. (1978) for optical probes, but none of them have tried to use this behaviour for velocity measurements: the former have developed bi-probes, the latter have proposed velocity measurements based on the signal amplitude. Also, we recently became aware that Sene suggested the possibility of performing gas velocity measurements using rise times in 1984. Using a crude model, Sene (1984) found that the duration T_u should be proportional to the velocity to the power $-3/2$. Such a trend was not confirmed by the experiments he performed on an optical probe, and it seems that this technique was not developed further. In order to perform accurate velocity measurements using the above principle, probe optimisation is required. First, since the accuracy of T_u is controlled by the time resolution of the detection and treatment system, L cannot be too small. To properly determine the duration of the transitions, adapted processing criteria must be defined: it is thus necessary to master the shapes of transients to optimise this procedure. Lastly, the correlation T_u (V_i) could be sensitive to random parameters which are not controlled during measurements in a two-phase medium, such as the local interface curvature a, the angle γ between the probe axis and the angle of impact on the interface β (Fig. 2). It has been shown that the angle β can alter the rise time by a factor as large as five, and to eliminate this source of error, meaningful transitions

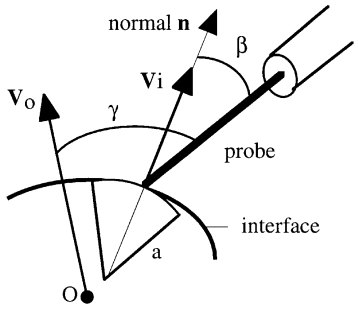

Fig. 2. Parameters involved in a two-dimensional probe/interface interaction.

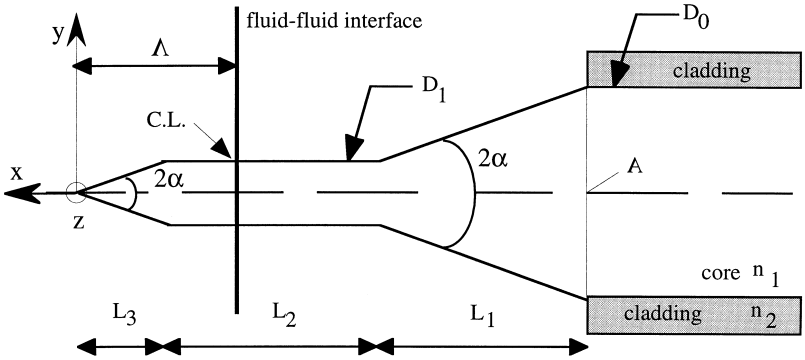

Fig. 3. Geometrical parameters defining the idealised fiber tips.

must be selected by signal processing (Cartellier, 1992). A reduction of such sensitivities is nevertheless highly desirable to achieve a much sounder technique.

This introduction clearly demonstrates that, for interface velocity measurement as well as for interface detection, a basic problem is to properly link the aspect and the duration of the signal transitions with the probe geometry and size. This paper is thus intended to bring some responses to this central question in the case of optical fibers. Emphasis is put on the definition of probe tips allowing a control of the latency length, with the practical aim of a simultaneous detection of gas inclusions and of their velocity. According to previous observations on stretched fibers (Cartellier, 1992 §IIA), a probe tip including a cylindrical portion is believed to be favourable for geometrical control of the latency length. Thus, geometries such as conical + cylindrical (hereafter referred as 2C) and conical + cylindrical + conical (hereafter referred as 3C) schematised in Fig. 3, will be considered in a companion article (Cartellier and Barrau, 1998), hereafter referred as part II). In this first paper, attention is focused on basic shapes such as cleaved fibers and simple cones (hereafter referred as 1C) which are commonly used in two-phase flow analysis. The paper is organised as follows: in the next paragraph, the tools needed for this study are presented: namely, the manufacturing technique whose reproducibility is discussed, the optical simulation and the facilities used for piercing experiments. Then, for cleaved tips and for 1C probes, simulations and experiments are jointly analysed. Finally, the ability of conical probes to provide gas phase velocity is discussed.

2. Investigation tools

2.1. Manufacture of probes and shape control

In order to conduct a combined analysis based on optical simulations and on experimental piercing tests, it is essential to be able to reproducibly manufacture the desired fiber tips. Let us briefly overview the available manufacturing techniques. The melting and stretching technique is now very popular. Although it has been improved in the past years, its reproducibility is not yet satisfactory (see Fig. 1), probably because the production relies essentially on personal skill. This limitation can possibly be overcome with industrial micro-pipette pullers classically used

in biology and neurology (Flaming and Brown, 1982); indeed, some preliminary tests we conducted with this device are encouraging. They allow production of very sharp tips (below 0.1 m) both for optical and impedance techniques, and so an optimisation specifically devoted to phase detection is foreseeable. However, the shapes adapted to the velocity measurements we want to conduct are difficult to obtain with this technique. Similar limitations are expected with an alternate technique, which consists of heating by a laser launched directly in the fiber with its tip oriented toward a special target: micro lenses or micro spheres of high quality are thus obtained (Russo et al., 1984). Since melting is involved in both cases, some cladding is left on the tip and it must be characterised before attempting a simulation. To avoid these difficulties, unclad fiber tips have been considered, despite the expected lower signal dynamics. Polishing is also a potential technique, which is notably used to shape laser surgery tools (Royston et al., 1989), but it is quite delicate when applied to sizes as small as a few tens of micrometers.

We finally decided to adapt an etching technique that is widespread in fiber optics technology. Thanks to a chemical attack by an acid, the cladding is indeed eliminated. The isotropy of this process facilitates the formation of cylinders, and its time scale, which is typically half an hour (the speed of attack is about a few micrometers per minute) is convenient for accurate control of the geometry. The conical shape results from the presence of a meniscus along the fiber during the manufacturing process: the final cone angle is a function of the surface tensions and of the contact angle (Takahashi, 1990). With this technique, we have been able to vary the half-cone angle within a limited range, namely $\alpha \in 11.5^\circ; 15.5^\circ$. Also, combinations of cones and cylinders are readily accessible: such shapes will be analysed in part II. Some realisations of conical probes are illustrated in Fig. 4. The reproducibility is quite good: the variance in α is about 2°; the cylinder diameter is controlled within a few micrometers, and the accuracy in length is set by the resolution of the translation mechanism ($\approx$20 μm in our conditions). In addition, it is possible to obtain very smooth surfaces with the etching process. In practice, some deviations could occur due to insufficient temperature control or lack of acid purity. But the main defect of this technique consits of distortion at the base of the first cone which could be quite strong as shown in Fig. 4(b). This could be attributed to a variation of the contact angle due to the difference of materials between the core and cladding, and also to hysteresis effects of this angle. Apart from this problem, this technique is well suited for obtaining the desired shapes, and its reproducibility is good enough to allow a systematic study of the influence of the geometry on the probe response. This is a necessary condition to achieve some progress in the understanding of the optical probe behaviour. Pinguet (1994) was faced with comparable difficulties for the impedance technique. His ability to manufacture reproducible sensors simple enough to be described by a finite number of parameters was also a keystone of his study.

2.2. Modelling of the optical response

Our objective is mainly to characterise the sensor response during the crossing of interfaces. Due to the involved time scales of optical and hydrodynamic phenomena, the signal issued from an optical fiber depends only on the instantaneous position of the interface. To predict the transients, the difficult hydrodynamic problem is discarded: the interface is idealised as a

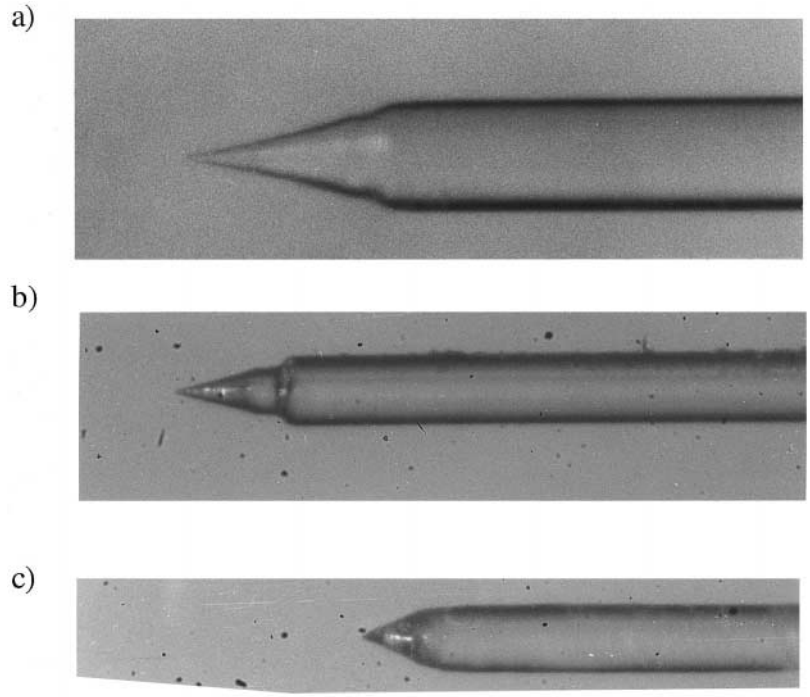

Fig. 4. Some probe tips produced by the etching technique: (the fiber external diameter at the right hand side of photographies is 140 μm).

plane wall always perpendicular to the fiber axis. This approach allows definition of the intrinsic detection capability of the sensor without reference to the surge effect, to drainage and to dewetting or wetting phenomena. Also, the geometric displacement velocity of the undisturbed interface provides a simple conversion factor between temporal and spatial scales. For this idealised situation, it is thus equivalent to consider the evolution of the signal with position Λ of the interface (Fig. 3) instead of its time variation.

The optical modelling is based on geometrical optics. This approximation is well suited for the step-index multimode fibers considered here. Diffraction can be neglected because the typical probe dimensions remain higher than a few tens of a wavelength. For multimode fibers, a high number of propagation modes simultaneously exist (Okoshi, 1982) which are dependent on various parameters such as the light injection conditions and the fiber curvature. This complex behaviour has been idealised by the introduction of a continuous model distribution sketched in Fig. 5: the unaltered fiber cross section located at the rear of the sensitive region of the tip is set as the reference plane (Ayz plane where the z axis is perpendicular to the figure), and it is assumed that each point of this reference cross section acts as a source emitting homogeneously in a sector of extent $-\Theta_m$, Θ_m, where Θ_m is related to the numerical aperture (N.A.) of the fiber (N.A.$^2 = n_1^2 - n_2^2$ where n_1 and n_2 are, respectively, the core and cladding refractive indexes) according to $\Theta_m = a\sin(\text{N.A.}/n_1)$. Indeed, any ray whose inclination θ with the fiber axis is higher than Θ_m should have been lost, provided that the fiber is long enough. It is assumed that all these secondary sources emit the same power, so that the light

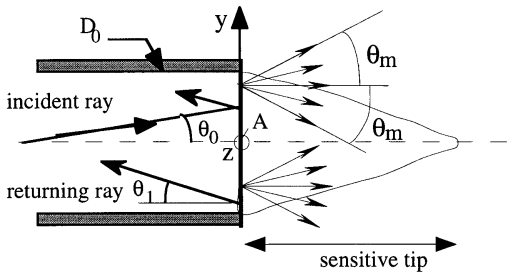

Fig. 5. Idealised light injection used in the simulation.

distribution remains axisymmetric. However, in order to simplify the approach, all skew rays are discarded so that the computations are made only in the meridian plane (x, y). Note that planar approaches have also been used by Vince et al. (1982) to optimise the signal amplitude for a high-temperature sapphire probe, and by Abuaf et al. (1978) for conical probes. In the meridian plane (x, y), an incident ray is thus defined by its launching conditions (y, θ), with the height $y \in (-D_0/2;\ D_0/2)$ and the inclination $\theta \in (-\Theta_m,\ \Theta_m)$. Denoting as P_0 the incoming light power available at the Ayz plane, each ray is associated with the same power density equal to $P_1 = P_0/(2\ \Theta_m\ D_0)$. Every time the ray impacts the fiber surface, P_1 is weighted by a reflection coefficient R', which is a function of the ray injection conditions y and θ as well as the position Λ of the liquid–gas interface. While Abuaf et al. (1978) have introduced an idealised reflection coefficient as being equal to one when total reflection occurs and to zero otherwise, the true magnitude of R' is considered here. For unpolarised light, R' equals unity when total reflection occurs, otherwise it equals half the sum of the reflection coefficients for an electric field parallel and perpendicular, respectively, to the incidence plane. Rewriting these coefficients (chapter 2, Okoshi, 1982), R' is found to be:

$$R' = \frac{1}{2}\left\{\left[\frac{n_1\cos\theta_i - n_e\cos\theta_t}{n_1\cos\theta_i + n_e\cos\theta_t}\right]^2 + \left[\frac{n_1\cos\theta_t - n_e\cos\theta_i}{n_1\cos\theta_t + n_e\cos\theta_i}\right]^2\right\} \tag{1}$$

where θ_i and θ_t are, respectively, the incidence angle in the fiber core and the refractive angle in the external medium (of refractive index n_e) with respect to the local normal at the fiber boundary. Taking into account all the reflections experienced by a given ray (y, θ), its power density R_i (y, θ, Λ) P_1 is computed when and if it crosses the reference plane with an opposite direction of propagation. Again, the guidance condition is checked to be sure that the returning ray is able to reach the detector: the contribution of rays whose inclination with the axis is larger than $\pm\Theta_m$ is discarded. The final result is an average reflection coefficient R computed over all rays guided back to the detector, which is a function of the interface position Λ according to:

$$R(\Lambda) = \frac{1}{2\,\Theta_m\,D_0}\int_{-D_0/2}^{D_0/2} dy \int_{-\Theta_m}^{\Theta_m} R_i(\Lambda, y, \theta)\,d\theta. \tag{2}$$

Absorption in the fiber being neglected, R represents the fraction of the incoming light intensity which returns to the detector. To evaluate R, the integration domain over (y, θ)

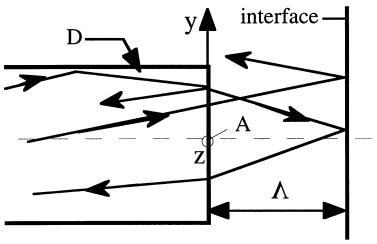

Fig. 6. Active rays responsible for proximity detection by a cleaved tip.

involved in [2] is discretized as about 100 positions times 100 angles homogeneously distributed over their respective intervals: each of these rays is subject to a standard ray tracing procedure. To describe the complete signal transient, the interface position Λ evolves from a slightly negative value (corresponding to total immersion of the probe in the first phase), to a value exceeding the total length L_T of the sensitive tip (corresponding to total immersion of the probe in the second phase); the interface position is moved typically in steps of 10 μm.

Since the signal is linearly related to R, the predictions of transients are expected to be valid in their form and their duration. But the predicted absolute amplitudes are probably less significant because of the planar approximation and because they are, in practice, sensitive to optical connectors, Y couplers, light injection conditions, fiber curvature, not to mention probe fouling. Besides, since any ray exiting the fiber core is completely lost, our modelling depends only on the position Λ of the contact line along the fiber tip (C.L. in Fig. 3). It is thus unable to take into account the actual shape of the interface, which can unpredictably alter the effective refractive indexes at the core/water interface (opposite trends appear in the simulations of Vince et al., 1982). Thus, the validity of the idealised model remains to be checked by comparison with experiments.

To improve the simulation of signal transients, a situation involving the contribution of rays exiting the fiber core has nevertheless been considered because experience shows that an interface can be perceived before the contact with the probe occurs. Since this so-called proximity detection can induce erroneous phase detections, its analysis is of practical importance. To treat this aspect, a fiber cleaved normal to its axis is considered ($L_1 = L_2 = L_3 = 0$). Although hydrodynamically not well suited, such cleaved tips are sometimes used (Morris et al., 1987), especially when a Doppler signal is exploited for interface velocity measurements (Sekoguchi et al., 1984; Podkorytov et al., 1989). As sketched in Fig. 6, this geometry is very favourable for proximity detection because all the frontal area collects the reflected light. Using the same assumptions as above, and neglecting absorption by air and water (Kent and Dudley, 1974), the evolution of the signal amplitude with distance from the tip to the interface is estimated by considering rays reentering the fiber after a reflection at the liquid–gas interface. A single reflection at the liquid–gas interface is taken into account. The computation of reflection coefficients now includes the transmission factors (given by $T' = 1 - R'$) between the fiber core and the external medium, and for the two directions of propagation. It also includes reflection at the boundary between the fiber core and the external medium.

The simulation of proximity detection is independent from the computation of transients involving a sliding contact line. Thus, for geometries such as the cleaved 1C probes and 2C

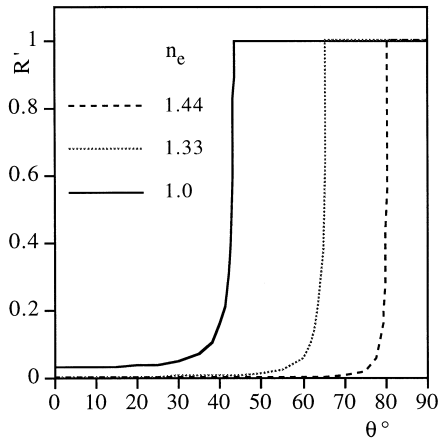

Fig. 7. Refraction coefficient at the boundary between the fiber core ($n_c = 1.46$) and various external media.

probes, the two predictions must be combined to get a complete simulation of transients during the piercing of planar interfaces.

Most simulations have been performed for a silica fiber with a core diameter D_0 of 100 μm, a core index n_1 of 1.46, and a cladding index n_2 of 1.44 so that the numerical aperture is about 0.24, and $\Theta_m \approx 9.5^\circ$. External medium is either air ($n_a = 1.0$) or water ($n_f = 1.33$), for which the critical incidence angles at the fiber core boundary are, respectively, 43.2° and 65.6°. The evolution of R' with the incidence angle for the medium considered here is plotted in Fig. 7. It should be mentioned also that, although D_0 has been fixed, the results are valid for any multimode fiber core diameter provided that the shapes are self-similar.

2.3. Piercing experiments: facilities

Various small-scale facilities have been used to study probe-interface interactions. They cover the four possible situations for probe-interface interactions. The most common are the water exit and the water entry, which correspond to the sequence of events for a probe immersed in a gas–liquid flow with its tip facing the mean velocity (i.e. $\gamma = 0^\circ$). The inverted situations can be met for a reversed gas velocity (i.e. $\gamma = 180^\circ$) when a large gas inclusion surrounding the probe slides along its support up to the tip. Although rare, these configurations are worth studying in view of a possible determination of the flow direction which is of high practical value.

Quasi-steady piercing is achieved by translating the probe through a steady interface: one obtains the signal evolution with the probe position relative to the undisturbed interface location, which is known with a 10 μm accuracy. Although sensitive to contact angle hysteresis, such tests are valuable for understanding sensor response. Since the interface deformation depends on the relative velocity between the probe and the interface, dynamic conditions are also investigated: they are obtained either by emptying a liquid column, in which case, the interface remains planar (at least below velocities of about 0.6 m/s), or by generating isolated slugs in small tubes which can provide velocities up to 7 m/s. These facilities and their performance are described in detail elsewhere (Cartellier, 1990, 1992). The above mentioned

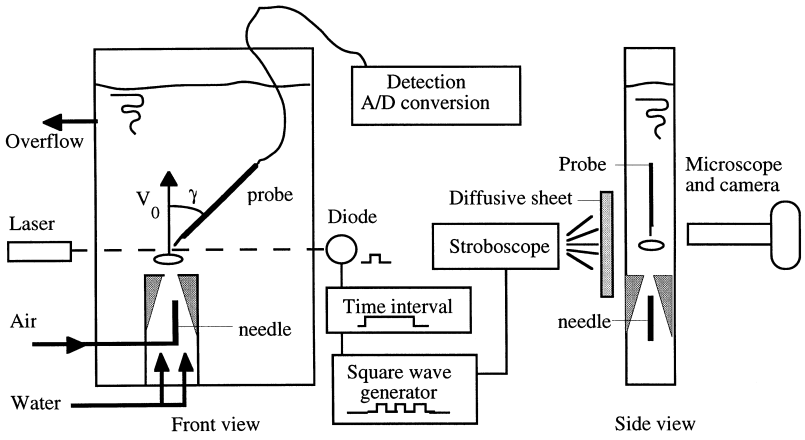

Fig. 8. Sketch of the piercing experiment.

experiments allow a study of the influence of the interface velocity V_i, the interface curvature a, and the angle of impact β.

A new experiment has been designed to study the effect of velocity orientation (angle γ) and to analyse the signatures associated with small bubbles cut at various eccentricities. The facility consists of a single air bubble generator (a needle of 90 μm internal diameter) immersed in water (Fig. 8). Typical bubble size is about 2 mm, a magnitude for which bubbles are ellipsoidal and experience helicoid trajectories in stagnant water. The injector is located inside a convergent nozzle supplied with a constant water flow rate, so that the bubble trajectory stays rectilinear over a short distance (10 to 15 mm) after the nozzle exit. The probe tip is located within this zone, at an angle with the vertical, i.e. with the bubble velocity vector, between 0° and 90°. The water flow rate provides a control of the magnitude of the bubble velocity.

To measure the bubble size, the velocity of its centre of mass V_o, as well as the angles γ and β, multi-exposure pictures of the tip region are taken under a microscope. A stroboscope is used for illumination with the total number of flashes and frequency controlled by home-made circuitry. This system starts when a bubble at the nozzle exit is detected by a photodiode while passing through a laser beam. A typical frame obtained with this technique is presented in Fig. 9. Simultaneously, the signal from the probe is digitized (up to 1 MHz, 10 bits). The optoelectronic detection device has a typical rise time of 1.2 μs at its minimum gain. A post-treatment gives access to the rise times for different threshold levels: these levels are usually chosen as 10% and 90% of the full-scale signal, but other values could be more appropriate according to the shape of the transition.

The presentation of tools being completed, let us turn now to the analysis of probe response.

3. Cleaved fiber and proximity detection

The special case of proximity detection is discussed first, since it also concerns cleaved conical probes presented in Section 4 and cone + cylinder probes presented in part II. The transients predicted by simulation of the detection of water–air and air–water interfaces

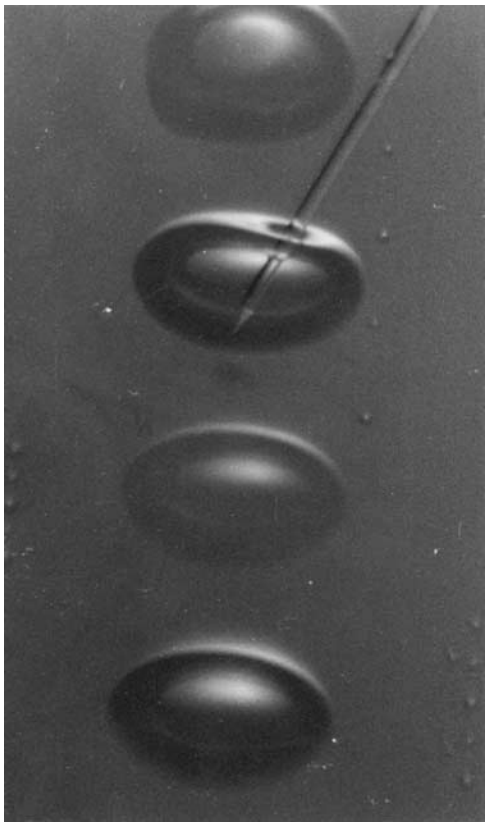

Fig. 9. Typical frame collected during the experiments (the fiber external diameter is 140 μm).

located some distance ahead of the tip are shown in Fig. 10. In the former case, the signal for a wetted tip starts at $R = 0.2\%$ for large distances. As Λ diminishes, additional light is collected by the fiber and R increases monotonically with decreasing Λ, approaching 2.2% as $\Lambda \to 0$. This level is close to that predicted by Morris et al. (1987) as equal to $R_{\text{glass–water}} + R_{\text{water–air}}\ (1 - R_{\text{glass–water}})^2$ where the reflection coefficients R are estimated for normal incidence. Then, since there is no interfacial deformation, the signal jumps instantaneously to the dry probe level as soon as contact occurs ($\Lambda = 0$). This final level computed as $R \approx 3.49\%$ fits the glass–air reflection coefficient estimated for normal incidence.

For an air–water interface, the probe response starts at 3.5% for a large distance Λ. Then the light reflected at the air–water interface is collected more and more by the fiber as Λ decreases: the amplitude increases monotonically up to $\Lambda = 0^+$, where R reaches 5.36%. Again, the same level has been deduced by Morris et al. from reflection coefficients for normal incidence, using the expression $R_{\text{glass–air}} + R_{\text{water–air}}\ (1 - R_{\text{glass–air}})^2$. As contact occurs at $\Lambda = 0$ in the absence of interface deformation, the signal drops to the liquid level, i.e. $R = 0.2\%$. Typically, proximity detection is efficient from a distance of about 10 times the core diameter for a tip approaching from the water side or the air side.

Both kinds of surges are observed in practice for cleaved fibers (see Figs. 9–11 part (II)). By progressively moving a cleaved probe perpendicularly towards a planar water–air interface,

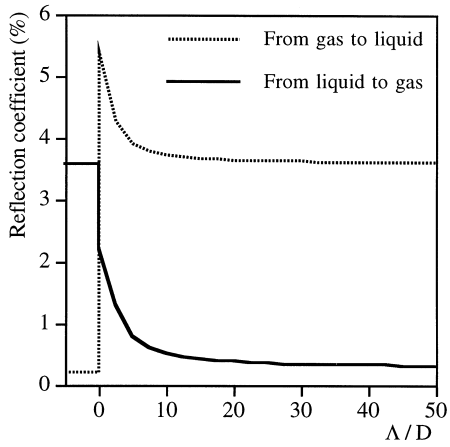

Fig. 10. Simulation of proximity detections for L/G and G/L interfaces approaching a cleaved fiber (N.A. = 0.24).

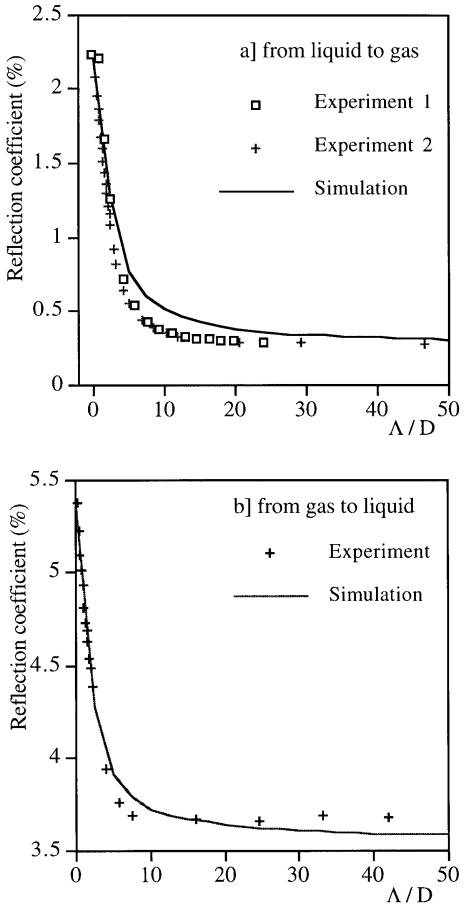

Fig. 11. Comparison of simulated and measured proximity detection (D = 58 μm).

proximity detection can be experimentally quantified. For comparisons with simulations, shown in Fig. 11(a) and (b), the distance Λ has been made dimensionless by the diameter D of the front cylinder (here $D = D_1 = 58$ μm). For ordinates, the actual signal in volts has to be transformed into a reflection coefficient R. The scaling is established with a linear relationship calibrated using two reference conditions, namely one for $\Lambda \to \infty$ and one for $\Lambda \to 0^+$. Clearly, the behaviour of the signal with the interface to probe distance is well predicted both for water entry and water exit conditions. The detection range is indeed about 10 tip diameters for the numerical aperture considered; slightly different values are expected for other apertures (Conley et al., 1986). These quantitative predictions can be helpful in defining a signal processing sequence for cleaved fibers, or whenever presignals appear (Schmitt et al., 1995).

4. Conical and cleaved conical tips

4.1. Simulations of 1C probes

4.1.1. Perfect conical tips

A perfect cone is uniquely defined by its tip half-angle α ($L_1 \tan \alpha = D_0/2$, $L_2 = L_3 = 0$ in Fig. 3). The signal is due to rays whose direction of propagation are reversed after a variable number of reflections at the fiber core/external medium boundary. The resulting amplitudes for a fully dry and a fully wetted probe are plotted vs α in Fig. 12. The reflection coefficient for water always remains very low ($< 0.05\%$), except in the range [80°, 90°] where the limiting case of a cleaved fiber is linearly approached ($R \to 0.22\%$ as $\alpha \to 90°$). The best sensitivity in detecting the presence of air or water is obtained for α close to 45°, a geometry often exploited after the pioneering work of Miller and Mitchie (1970). Lower tip angles are considered inefficient for phase detection by Vince et al. (1982) and by Abuaf et al. (1978). An opposite conclusion is obtained here, although the difference between the air and water reflection coefficients strongly decreases as tips become sharper. This loss of signal is due to the increase in the number of impacts necessary for a ray to come back, and also to the partial reflections

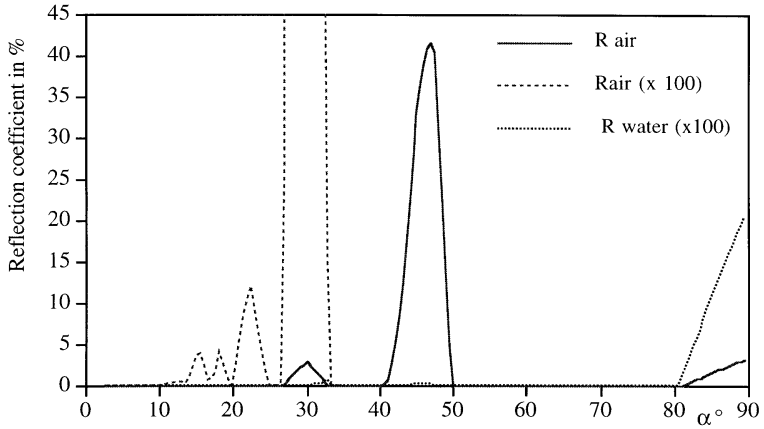

Fig. 12. Predicted static air and water levels for perfect cones as a function of the tip half angle.

involved in this process. Efficient tip angles are distributed in well-defined intervals around local maxima located at 30°, 22.5°, 18°, 15° and 12.8°. This curious behaviour can be recovered through simple arguments. Let us consider a ray launched with an inclination θ_0 with the fiber axis. At the first impact on the cone, its incidence is $\pi/2-\alpha-\theta_0$, and for every additional impact in the forward direction of propagation (toward the tip or $x>0$), its incidence diminishes by an amount of 2α. After N impacts in the forward direction, the incidence is $\theta_N = \pi/2-(2N+1)\alpha-\theta_0$. When θ_N becomes less than the tip angle 2α, the direction of propagation is reversed; the ray travels now towards $x<0$. The first impact after this reversing is done at an incidence of $2\alpha-\theta_N$. Thereafter, each time the ray impacts the cone in the backward direction, the incidence angle increases by 2α. Denoting K the total number of impacts during the backward propagation, the ray returns in the fiber core with an inclination θ_1 equal to $\pi-2\alpha(N+K)+\theta_0$. This ray reaches the receiver if the condition $-\Theta_m \le \theta_1 \le \Theta_m$ is fulfilled. Since the injection imposes that $-\Theta_m \le \theta_0 \le \Theta_m$, combining these inequalities leads to $-2\,\Theta_m \le \pi-2\alpha\,(N+K) \le 2\,\Theta_m$. This condition means that for a given angle α, only some rays subject of a well-defined number of reflections can return through the fiber. In other words, efficient tip angles should lie in the intervals $[(\pi/2-\Theta_m)/(N+K);\ (\pi/2+\Theta_m)/(N+K)]$. For integer values of $N+K=P$, the centres of these intervals are located at $\pi/(2P)$ and correspond to the maxima predicted in Fig. 12. Also, a single impact ($P=1$) corresponds to a cleaved fiber ($\alpha=90°$). Similarly, the widths of these intervals, i.e. $2\Theta_m/P$, agree with the computed values at $\alpha=45°$ for $P=2$, at $\alpha=30°$ for $P=3$ and at $\alpha=22.5°$ for $P=4$. At $P=1$, only half of the interval appears in Fig. 12; it starts as expected at about $81° \approx 90°-\Theta_m$. Each of the above maxima are associated with a single family of active rays defined by a fixed number of impacts P. For a given value of P, various combinations of the numbers of forward N and of backward K impacts are possible, but, due the symmetry of tips, the difference between N and K is limited to 0 or 1. For a number of impacts above 5, the corresponding α intervals overlap; that means that rays subject to different numbers of impacts are simultaneously active. This overlapping increases with Θ_m and so does the difference between air and water reflection coefficients. At all angles, high numerical apertures are therefore recommended for unclad conical tips.

It is interesting to note that, for the family of conical tips whose half angle is close to 45°, P equals 2 and the most active rays, which are such that $N=K=1$, experience total reflection. This family of conical tips is the only one for which total reflection occurs, and corresponds indeed to the highest sensitivity. Thus, the classical presentation of the optical probe behaviour found in many books or articles, based on a single ray parallel to the fiber axis and twice totally reflected, provides a correct picture for this particular geometry.

Let us note also that the high signal change between air and water with sharp stretched probes is due to the presence of the cladding which concentrates the light at the tip, and this situation is not comparable with the above conditions.

This simulation shows that unclad sharp tips, favourable for interface penetration, are also suitable for phase detection. The water exit transitions have been computed for some optimum angles, and typical results are plotted in Fig. 13. For α close to 45°, the signal is a linear function of the dewetted length Λ. The whole cone contributes to the signal so that the latency length fits exactly the tip size L_1. This prediction is confirmed by the experiments of Abuaf et al. (1978) on an edge probe designed at $\alpha=45°$; they measured a latency length of 240 μm for a tip length of 250 μm. At smaller angles, the predicted transitions are nonlinear functions of Λ

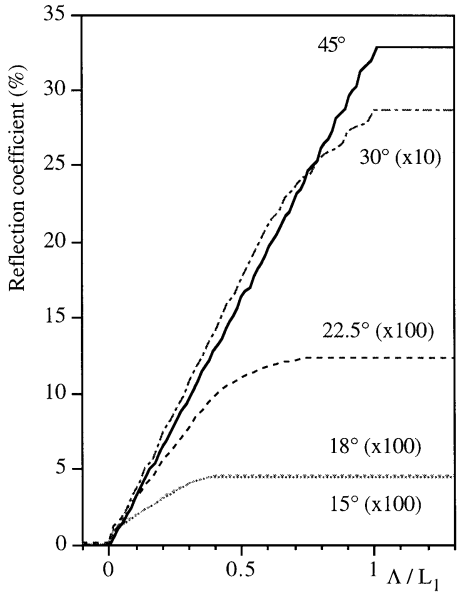

Fig. 13. Transients predicted for perfect conical tips.

and the sensitivity length becomes shorter than the tip length. For α less than about 20°, L is less than half the cone length L_1 and there is no contribution from the cone base. This is because, for such sharp tips, active rays must travel closer to the extremity before they can return back. Latency lengths are quantified in Table 1 for various angles. Two characteristic lengths are given, namely L10–90 defined between the 10 and 90% thresholds, and L0–100 defined between 0 and 100%, which is the magnitude of the entire sensitive length. No clear relationship appears between the physical dimensions and the latency lengths except at large angles. Besides, for small tip angles, angle variations as small as 0.5° or 1° produce significant changes in sensitivity lengths. Such a sensitivity precludes the blind use of simulations for the determination of effective latency lengths of 1C prototypes since manufacturing processes do not allow a refined enough control of the geometry.

4.1.2. Cleaved conical tips

The sensitivity lengths analysed hereabove provide only a limited picture of the response of sharp conical probes. Indeed, another crucial aspect of these responses is the fact that the signal change is mainly due to the first 10 to 20 μm of the tip extremity. For example, the first

Table 1
Simulated latency lengths for perfect conical probes

Alpha°	45	30	22.5	18	16	15	14	13	12.5
L1 μm	50	86.6	120.7	153.9	174.4	186.6	200.5	216.6	225.5
L10–90 μm	45	44	59	48	35	52	70	40	50
L0–100 μm	50	85	105	70	44	68	92	69	88

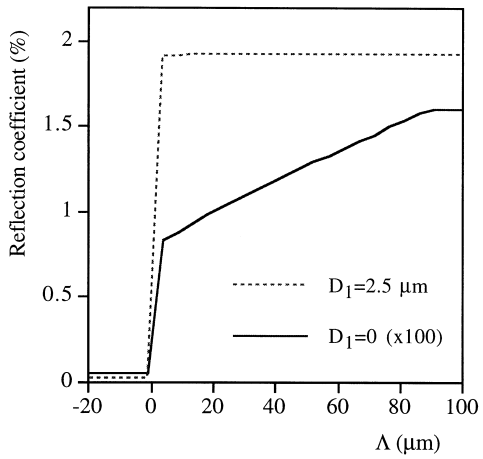

Fig. 14. Influence of a cleaved end on transients ($\alpha = 14°$).

steep surge represents 50% of the full output obtained with a perfect cone at $\alpha = 14°$ (Fig. 14). One can thus anticipate a high sensitivity of the response to the actual tip geometry, since, whatever the involved manufacturing technique, small deviations from a true cone are expected at the extremity.

To study the influence of such imperfections, cleaved conical tips, which are sometimes used for phase detection, have been considered. This geometry is defined by α and by the diameter D_1 of its flat end [$2\ L_1 = (D_0 - D_1)/\tan\alpha$; $L_2 = L_3 = 0$]. Compared with perfect cones, the peak signal output is higher; as shown in Fig. 14 for $\alpha = 14°$, the signal amplitude increases up to 1.9% for a tiny flat tip $D_1 = 2.5$ μm instead of 0.01% for a perfect cone. Note also that, at low tip angles, almost all the signal is produced by the cleaved end. The influence of the cleaved diameter D_1 on the reflection coefficient (roughly the peak signal), shown in Fig. 15 for

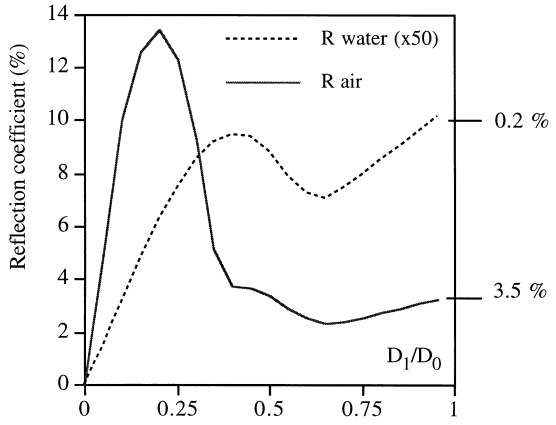

Fig. 15. Influence of the cleaved size on signal amplitude ($\alpha = 14°$, $D_0 = 100$ μm).

$\alpha = 14°$, demonstrates that phase discrimination is possible with any of these geometries. To understand this behaviour, active rays must be separated in three populations:

1. population 1 consisting of rays directly impacting the flat end; their average reflection coefficient is about 3.5%, and their relative contribution to the gas level increases with D_1;
2. population 2 formed by rays subject to the reversing process due to reflections on the cone sides and which do not touch the flat extremity; their contribution, which was already estimated during the analysis of perfect conical tips, is always weak except for α close to 45°;
3. population 3 corresponding to rays impacting the flat end after some deviation by the cone sides; their contribution is a function of α and D_1.

Large flat ends favour the first population which, above some critical defect size (about 65 μm for $\alpha = 14°$), overwhelms the other contributions. Thus, the signal becomes proportional to D_1, and approaches the limiting values for a cleaved fiber as $D_1 \rightarrow D_0$ as shown by Fig. 15. This holds at all α except in the vicinity of 45° where the second population remains the most efficient. Indeed, for 45°, the reversing phenomenon with total reflection takes place all along the cone, and by cleaving the extremity, only a few such rays have their path disturbed. Consequently, provided that D_1 remains smaller than D_0, a geometry with $\alpha = 45°$ is weakly sensitive to a tip defect. This observation strengthens the agreement on latency length underlined above between simulation and experiment for this peculiar geometry.

The other limiting case is that of a very small defect, in which case the second population is the only one active; as $D_1 \rightarrow 0$, the response of a perfect conical fiber is recovered.

Between these two extremes, i.e. in the general case, the main contribution is due to the third population. Instead of the limited amount of efficient rays involved in the response of a perfect cone, the presence of the flat end now increases the number of acceptable ray paths. Indeed, due to the reflection condition at this extremity, the inclination θ_1 of the returning ray as a function of the incidence angle θ_0, is now given by $\theta_1 = 2\alpha(N - K) + \theta_0$ (where N and K still denote the number of impacts on the cone for forward and backward propagations, respectively). Since the case $N = K$ provides some of the solutions, no condition is imposed on the angle α and all cone angles are eligible for phase discrimination. Additionally, some rays are now subject to total reflection when impacting the flat part because their incidence, given by $\theta_0 + 2N\alpha$, can exceed the critical angle at the fiber core/air boundary. Thus, compared to a perfect cone, the signal change between air and water is increased. Also, as the size of the flat end is enlarged, the number of required reflections for a ray to come back diminishes and the average reflection coefficient R is higher; this trend is confirmed by the simulations performed for $\alpha = 14°$ which predict an increase of R with D_1 until $D_1 = 20$ μm in air and 40 μm in water (Fig. 15). However, if D_1 is further increased, the number of rays pertaining to this population, whose existence is closely related to a deviation by the conical sides, is reduced to the benefit of the first population i.e. rays directly impacting the flat end. The competition between these two populations leads to a pair optimum for reflection coefficients, as shown by Fig. 15 ($R \approx 13\%$ at $D_1 = 20$ μm). Also, as the angle of a perfect cone diminishes, the rays must travel further along the tip before reversal occurs. Thus, as the tip sharpens, the influence of a cleaved

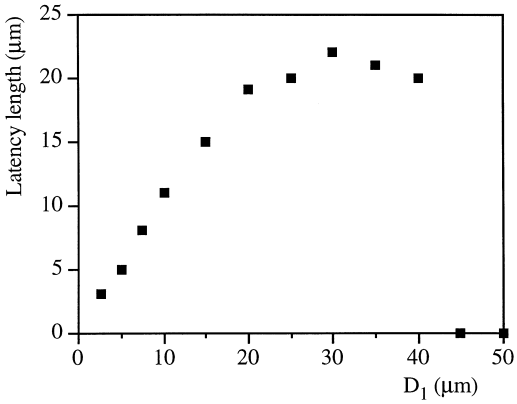

Fig. 16. Predicted latency length evolution with D_1 for a cleaved conical tip ($\alpha = 14°$).

extremity will be sensed starting from a lower "defect" size. This behaviour is also confirmed by simulations.

In parallel with the changes in R, the cleaved cones provide steeper transients during liquid-to-gas transitions, and the latency length drastically decreases. For $\alpha = 14°$, it drops from about 90 μm for a perfect cone to less than 5 μm for a diameter D_1 equal to 2.5 μm (see Fig. 14). As the defect increases, the response becomes similar to that of a cleaved fiber, and above a critical size, the transition is instantaneous and no latency length is left; this behaviour is exemplified in Fig. 16 where the limiting value of D_1 is close to 40 μm for a half cone angle of 14°. At low defect size, the latency length evolves also with α; the trend is a decrease of the latency length as the angle is increased, for a fixed cleaved diameter (Fig. 17). The evolution of L is not regular, and, again, it cannot be easily related to the geometrical tip length.

Let us now briefly describe the shape of transients predicted for the water entry problem. Examples are given in Fig. 18 for a perfect cone and a cleaved cone for a half tip angle of 14°. Again, the transition is achieved along a distance of 50 μm for a perfect cone, but a tiny defect renders it almost instantaneous.

It should be finally mentioned that in all the above simulations, a change in the numerical aperture and thus in Θ_m can modify the peak amplitude, but the durations of the transients are not affected. This is illustrated by Fig. 19 for $\alpha = 14°$, and for two apertures, namely 0.24 and 0.4 (the numerical aperture could be as large as 0.6 for silica fibers).

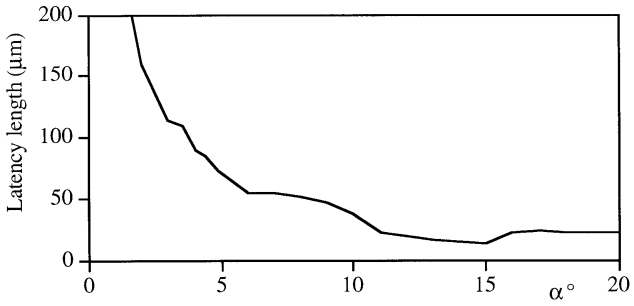

Fig. 17. Evolution of the latency length with tip half angle for a fixed cleaved size ($D_1 = 15$ μm).

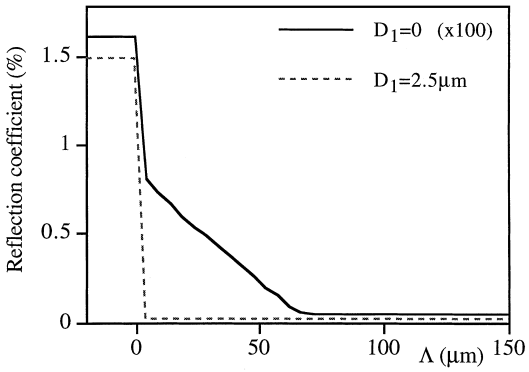

Fig. 18. Predicted water entry responses for conical and cleaved conical tips ($\alpha = 14°$).

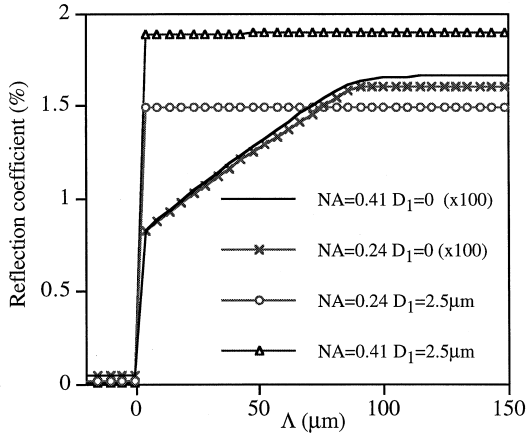

Fig. 19. Influence of the numerical aperture on water exit responses for cleaved conical tips ($\alpha = 14°$).

We have seen that cleaved conical probes provide a larger signal change between air and water compared to true cones, and are well adapted for phase detection. However, the latency length remains quite small and, as for perfect cones, they are sensitive to small geometrical variations. In view of velocity measurements, the control of latency lengths on prototypes with such shapes appears quite delicate. Another problem should be mentioned—such flat tips favour proximity detection which will be more pronounced as the size of the defect increases. The only situation weakly sensitive to tiny tip defects and thus potentially less subject to proximity detection is for α about 45°.

4.2. Experiments and discussion

The limited range of tip angles that can be manufactured with the etching technique prevents us from conducting a systematic comparison between simulations and experiments. Thus, the discussion is restricted to the case $\alpha = 14°$ which is the value obtained for most of our prototypes depicted in Table 2.

Table 2
Some characteristics of manufactured conical probes

Probe number	Length L1 μm	Tip half angle°	Comments
1C02	270 ± 20	14	Small defect at cone base—"dirty" probe
1C03 photo 4(a)	240 ± 20	14	Small defect at cone base
1C07 photo 4(c)	100 ± 20	22–27	Large defect at cone base—unsymmetrical
1C08	255 ± 20	14	Tiny defect at cone base
1C09 photo 4(b)	236 ± 20	15	Large defect at cone base along 70 μm
1C10	295 ± 20	12.5	Small defect at cone base along 30 μm

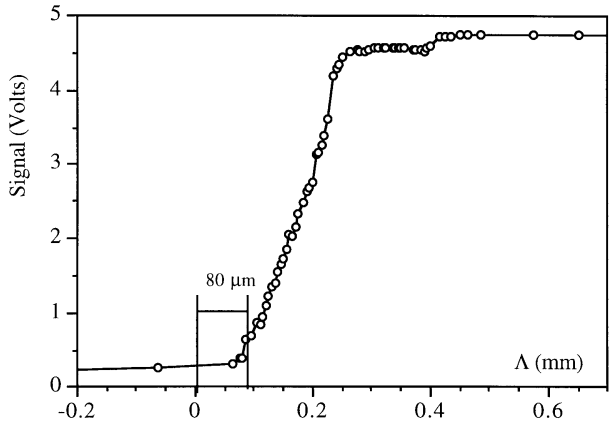

Fig. 20. Quasi-steady response of probe 1C02 during water exit ($\gamma = \beta = 0°$).

4.3. Quasi-steady piercing

Let us consider first some responses obtained under quasi-steady piercing perpendicular to a planar interface. A typical response for the probe 1C02 (Fig. 20) shows that the transition is monotonic. Prior to the main ramp, the signal increases slightly over 1% of the full amplitude gap, so that, within the experimental error, one can consider that this sensor is free of proximity detection. Then, a steep surge seems to occur at the very beginning of the ramp, possibly corresponding to the predicted surge, although its amplitude is much weaker than expected. Then, the signal increases almost linearly with the interface position up to a first plateau, followed by another surge of weak amplitude whose location is that of the geometrical defect at the base of the cone (see Section 2-A). The principal ramp corresponds to a displacement of about 170 µm, which means that the transition is almost completed within the first half of the tip, as predicted. The main difference between the experiment and the idealised

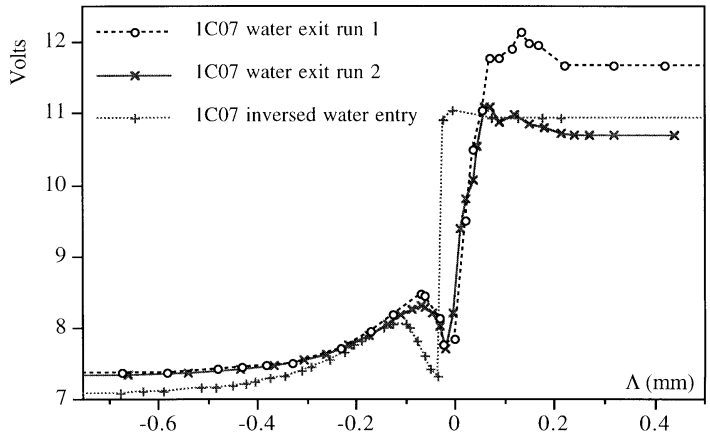

Fig. 21. Quasi-steady responses for probe 1C07: water exit and inversed water entry.

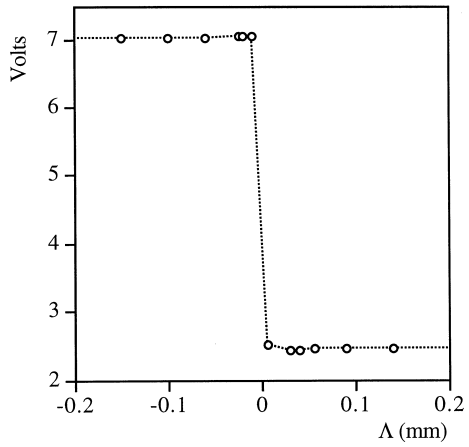

Fig. 22. Quasi-steady response for probe 1C07 during water entry.

simulation is that the start of the main ramp is located at about $\Lambda = 80$ μm instead of 0; this delayed response, due to fouling, will be discussed at the end of this section.

Similar tests, shown in Fig. 21, have been done for probe 1C07 whose tip is strongly distorted due to some problem during the manufacturing operation. The actual tip angle exceeds 20° and is not axisymmetric (see Fig. 4(c) and Table 2), and the base cone defect is strong, extending more than 50 μm. The two runs for a water exit configuration are very similar, except for the gas plateau level; they exhibit a first maximum prior to the contact with the interface, as well as a maximum at the end of the ramp. The main ramp starts at $\Lambda = 0$, as expected for a cone. The third run corresponds to an inverted water exit; the vertical probe, initially immersed in water with its tip in air, is progressively moved downwards. This run exhibits the same trends as the water exit response; the only difference is a shift in position because of the inverted meniscus obtained in this case. The maxima at the end of the transition are due to the geometrical distortion located at the rear of the tip. The response observed for negative values of the distance Λ is due to proximity detection but, instead of the continuous increase observed with cleaved fibers (see Section 3), a local maximum now appears when the interface is about 70 μm ahead of the probe tip. This non-monotonic evolution is due to the focalisation of light induced by a conical geometry (Royston et al., 1989). The differences between the responses of the probes 1C02 and 1C07 confirm what was expected from the simulation; tip imperfections have a huge influence on the shape of transients. They could result in proximity detection for conical probes, and the presence of a peak preceding the liquid-to-gas ramp is the signature of this effect. Such presignals have also been observed with 45° conical probes (Schmitt et al., 1995).

Few quasi-steady piercing tests have been performed for the water entry configuration. The example given in Fig. 22 for probe 1C07 is representative of the transitions observed with conical probes. The abrupt rupture occurs in the vicinity of $\Lambda = 0$ μm and is completed within 15 μm (the spatial resolution is 10 μm). This behaviour agrees with simulations, although in practice the wetting character of the water speeds up the transition. One can notice that for probe 1C07, proximity detection is almost undetectable during water entry, while it was an essential feature of the response during water exit. This behaviour is connected with the

interface deformation which, in the latter case, is important enough to act as a spherical mirror, and to concentrate the reflected rays inside the fiber. In the former configuration, the deformation is negligible, and the coupling in the fiber is less efficient. Thus, whatever the actual shape of their tip, the conical probes provide an accurate detection of the end of a gas inclusion, easy to identify for signal processing.

4.4. Moving interfaces

Let us consider now the responses for moving interfaces. Controlled piercing experiments have been achieved on isolated slugs and for various conical probes. The conditions of impact are normal ($\gamma = \beta = 0°$) so the magnitude of the interface velocity is that of the slug velocity. Note that the signal amplitude can vary by a factor 3 from probe to probe, which again demonstrates the huge influence of small geometrical variations on conical probes. Some water to air transitions are given in Fig. 23 for various velocities. Their shapes are similar to those observed under quasi-steady conditions. Indeed, for probes 1C08 and 1C10 whose geometry is very close to an ideal cone, transitions are monotonic regardless of velocity; the only difference is a weak overshoot located at the end of the ramp. Instead of the initial steep surge predicted for perfect cones, the beginning of transitions are rather smooth, an effect probably due to the rounded shape of the actual tips as well as to the interface deformation. For the distorted probe 1C07 subject to proximity detection, pre-signals are also present under dynamic conditions (Fig. 24); their amplitudes could even exceed the gas level. However, pre-signals are usually not detected for high slug velocities. This is due to fluctuations of the incidence angle β due to an oscillating interface; as β increases, the light collection is less efficient and the pre-signals become much weaker than for a normal incidence. A similar behaviour occurs in two-phase flows.

An overshoot is very often present at the end of the liquid-to-gas transitions, with the amplitude varying with the probe considered and, to a lesser extent, with the velocity. Using

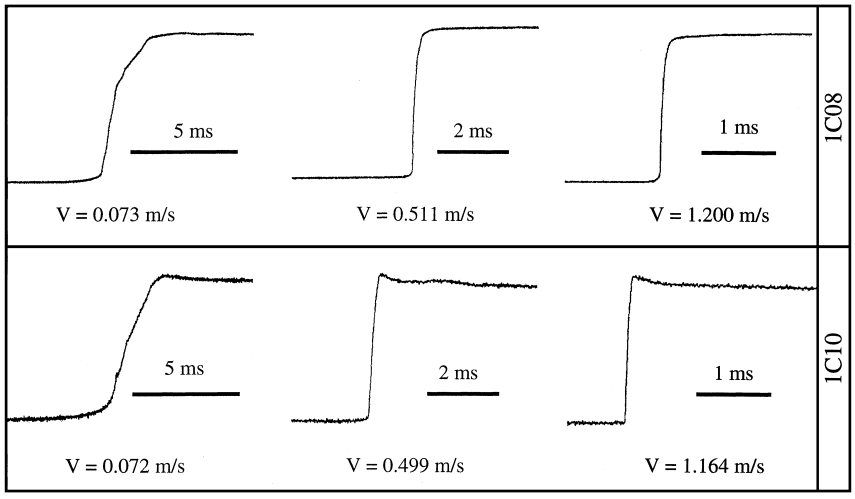

Fig. 23. Water exit responses for probes 1C08 and 1C10 (the time increases from left to right).

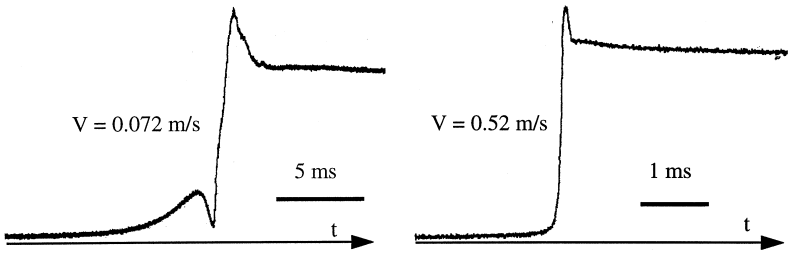

Fig. 24. Water entry transients for probe 1C07.

the signal records and translating the time axis into a length, it appears that such events are induced by the geometrical deformation present at the base of the cone on all 1C prototypes. The amplitude of the overshoot increases with the sensor distortion. It must be mentioned that similar maxima have been observed for stretched probes (Cartellier, 1990) and for a polished-edge probe (Abuaf et al., 1978). Since these geometries are less distorted than the conical probes studied above, it is possible that the overshoot is also controlled by a specific interface deformation occurring at the boundary between the conical and cylindrical portions of the probes.

The above discussion enlightens a limitation of our manufacturing technique. Indeed, some prototypes are subject to proximity detection while others are not (or at least the presignal is too weak to be detected) while no tip defect is perceived with a standard microscope. Thus, it is impossible to control and foresee the existence of a presignal in the response of a probe without the help of a piercing test for every new sensor.

4.4.1. Duration of transients

Although the above comments have demonstrated that a detailed understanding of the transitions is hard to achieve without considering hydrodynamic effect, the main features of the signal transients are captured by the idealized simulation. It is thus legitimate to analyse now the duration of the transients. Rise times are defined by setting lower and upper thresholds on the signal amplitude so that the very beginning and very end of the transitions are ignored. These thresholds are defined as a percentage of the amplitude gap between the constant liquid and gas levels obtained at each run. A wet probe provides the same signal level either in static or in dynamic conditions. For the gas level, however, there is always a difference between a fully dry probe and the levels obtained during dynamic experiments, probably due to some water retained on the surface in the latter case. This is the reason why the gas level has been evaluated for each test. For the discussion, instead of durations we will consider latency lengths, defined as the product of the rise time by the interface velocity.

For probe 1C10, which is not subject to proximity detection, the latency length for normal impacts ($\gamma = \beta = 0^\circ$) is plotted vs the slug velocity for various thresholds in Fig. 25. For a fixed velocity, the typical dispersion in rise times is about 5–8%. Part of this dispersion is due to a lack of control of the slug incidence angle, occurring mainly at high velocities for which the nose of the slug becomes asymmetrical. Whatever the threshold levels considered, the evolutions $L(V)$ are similar, and the behaviour of the latency length previously identified for stretched probes (Cartellier, 1990) is recovered. Above a critical velocity, which is here about

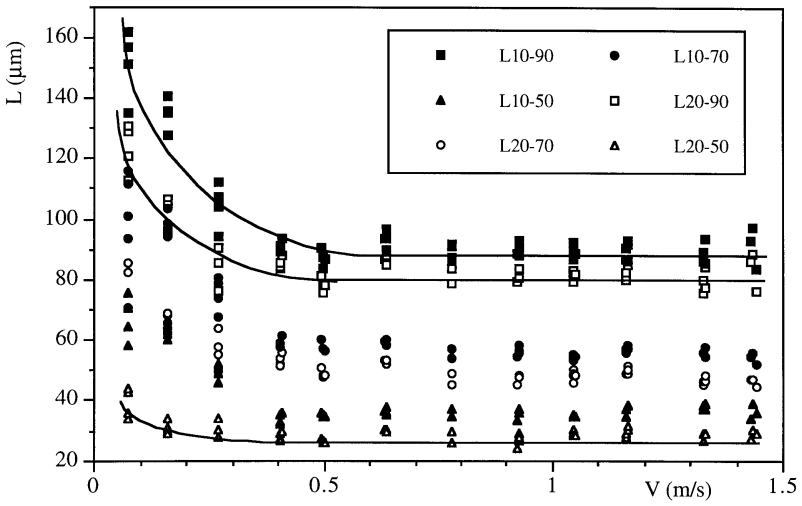

Fig. 25. Latency length of probe 1C10 for various upper and lower thresholds.

30 cm/s, the latency length is fairly constant. Denoting L^* this constant, the transient duration is thus equal to the transit time L^*/V. The sensor works like a time-of-flight technique acting over a distance L^* along the cone starting from its tip. Below the critical velocity, the drying process is longer than the transit time because the contact line dynamics come into play. In this low velocity range, the dispersion in transition durations is higher (typically 200 µs), a phenomenon related to contact angle sensitivity to local conditions and notably to the state of the fiber. It can be observed in Fig. 25 that, for a fixed upper threshold, the rise time remains closer to the transit time L^*/V when the lower threshold is 20% instead of 10%. Thus, the perturbation of the probe response due to the contact line dynamics affects essentially the contribution of the very tip of the probe.

Also, by examining in detail the evolutions of L at high velocities, it seems that for threshold levels of 10–90 (or 20–90) which integrate almost all the transient, L remains fairly constant, but for all other thresholds, starting with 10–80, L decreases slightly with velocity. In that case, the hydrodynamics is expected to control the film thickness evolution, and different behaviours between the very tip and the remaining conical part are expected.

Despite the influence of the actual tip geometry, the reproducibility of the latency length from probe to probe is not too bad, as shown in Fig. 26. In particular, probes 1C08 and 1C10 have similar latency lengths (see Table 3). Probe 1C09 exhibits quite a different trend since its latency length computed between 20 and 80% is steadily increasing with velocity. This is due to the important geometrical defect at the base of the cone [see Fig. 4(b)], which influences the second half of the transients. Indeed, when considering a latency length defined between 10 and 50%, this increase is much less pronounced. The influence of threshold values can be better appreciated from Fig. 27 where an averaged limiting value of the latency length $\langle L^* \rangle$ is plotted vs the upper threshold. For a given probe and thresholds, $\langle L^* \rangle$ has been determined as the mean value of all data collected above the critical velocity (which has been set to 0.3 m/s for all the probes). Clearly, the response between 10 and 90 or 20 and 90% is singular for probe 1C09. In all other cases $\langle L^* \rangle$ is close to an increasing linear function of the upper threshold for

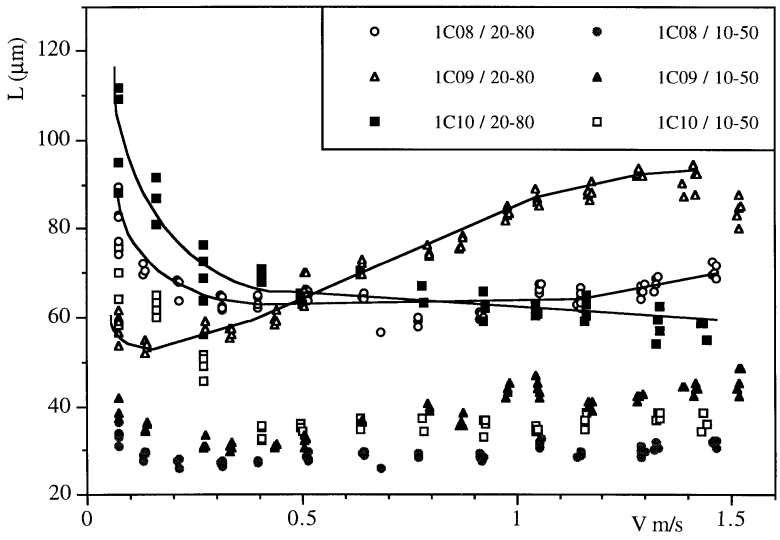

Fig. 26. Reproducibility of the latency length for conical probes.

a lower threshold of either 10 or 20%. That means that the responses of all conical probes are self similar, and smoothly related to the interface position along the cone. In the prospect of velocity measurements deduced from the signal rise durations, some freedom is left in the choice of adequate threshold levels, so that it is possible to eliminate signal distortions induced by nonideal probe geometry.

For conical probes not subject to proximity detection, absolute values of L^* are given in Table 3 together with predicted values for perfect cones. Despite similar magnitudes of the latency lengths, there is no close agreement between observations and predictions. Such a comparison is difficult to perform on a sound basis owing to the sensitivity of the predicted latency length to the tip angles combined with the nonideal geometries generated in practice. Besides, hydrodynamic phenomena, not taken into account in the simulation, are expected to be partly responsible for these discrepancies.

When considering probes subject to proximity detection, the latency length can include a portion of pre-signals if the threshold is too low. Since the amplitude of the pre-signal peak varies with the velocity and angle β, an automatic detection of rise times is risky. This is exemplified in Fig. 28 by the odd evolution of the latency length with velocity for probe 1C07.

Table 3
Comparison of predicted and measured latency lengths for 1C probes

	< —	Measurements	———— >	< —	Simulation for	perfect cones — >
	α°	L* 10–90 (μm)	L* 10–80 (μm)	α°	L* 10–90 (μm)	L* 10–80 (μm)
1C08	14	106	72	14	70	50
1C09	15	191	88	15	52	46
1C10	12	90	71	12.5	50	35

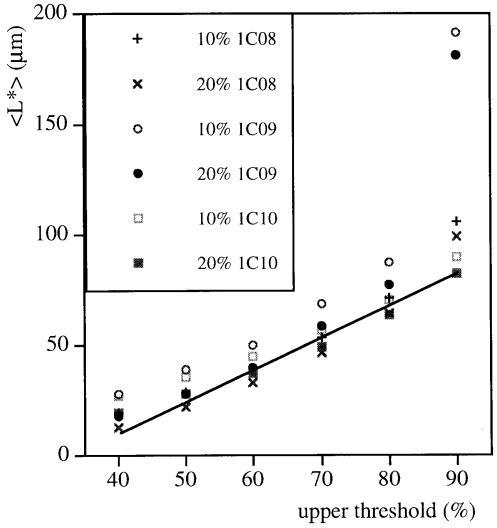

Fig. 27. Evolution of the latency length with thresholds for various 1C probes: (the lower threshold is given in the legend).

In view of gas velocity measurements, it is thus highly desirable to avoid any proximity detection. By comparing the latency length of this probe to the simulation of cleaved cones, the predicted trend is respected since L^* diminishes below 50 µm instead of being about a hundred micrometers as expected for a perfect cone. However, the tip defect is not quantifiable so that a more detailed comparison with simulations is not possible.

4.4.2. Dewetting and probe cleanliness

Although the process of dewetting is outside the scope of this paper, it is worthwhile to discuss some scenarios with the above observations. A first striking aspect, which holds even if

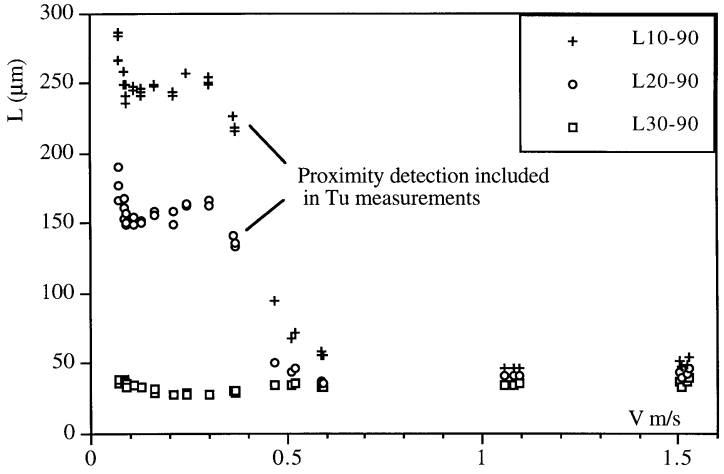

Fig. 28. Influence of the proximity detection of latency length measurements (probe 1C07).

the phenomena occurring at the beginning and the end of transitions are discarded, is that the measured latency lengths are always longer than those predicted by the idealised simulation. Such a delay of the detection can be attributed to the presence of a liquid film or meniscus which lags behind the undisturbed interface position (Billingham and King, 1995). Indeed, according to the evolutions of L with velocity, two dewetting regimes can be distinguished. Below a critical velocity of about 0.3 m/s, the surge of the interface is almost negligible (using a potential model, the deformation of the interface before the contact is less than 8 μm at 0.3 m/s for the conical probes considered here—Machane and Canot, 1995) and, after film rupture, the liquid meniscus is mainly controlled by the presence of the three-phase line. At higher velocities, the surge of the interface is roughly proportional to the velocity, about 30 μm at 1 m/s (Machane, 1996). In this case, the contact line is no longer the governing factor; according to the observations of Quéré (1991), instead of a liquid wedge, a thin liquid film is expected to be left on the solid. Its thickness, which varies with the capillary number $Ca = \eta V/\sigma$ and the Weber number $= \rho V^2 D/\sigma$ (where η is the dynamic viscosity, ρ the density, σ the surface tension, and D a characteristic probe size), is expected to always exceed a few micrometers for the probes considered here. Assuming a water film either parallel to the solid surface or inclined toward the probe tip, and following the history of an active ray for a sharp tip (say $\alpha = 14^\circ$), it is straightforward to show that a large amount of energy is lost compared to a dry fiber. Thus, for sharp tips, any kind of liquid film compatible with dewetting is expected to induce a lower signal amplitude than an ideally plane interface. Consequently, to reach a given amplitude, the undisturbed interface must travel further when a liquid film is present, explaining why the experimental or apparent sensitive lengths are longer than the simulated ones.

It is also interesting to provide some comments about the effect of probe cleanliness. Only a few tests have been carried out for the conical probe 1C03. The cleanliness of the probe has not been quantified; it has been checked qualitatively by observation through a microscope to visualise small solid particles attached to the surface. A comparison of signals shows that a clean probe exhibits a maximum at the end of the rising ramp, while for the same but dirty probe, the transitions remain smooth and monotonic. However, as shown in Table 4, the rise times between 10 and 90% levels remain approximately identical. This holds for a normal impact ($\gamma = \beta = 0^\circ$), as well as for an incidence of 30° ($\gamma = \beta = 30^\circ$). In the latter case, the difference in T_u is about 15%, but it is not significant because the relative uncertainty of T_u measurements was about 20% due to a very poor SNR when fouling is present. Also, the position of the probe impacting ellipsoidal bubbles is subject to variations which cannot be fully ascertained from the frames (see Fig. 9); this lack of control is responsible for deviations of T_u up to 15% from the mean in a given data series.

Table 4
Latency length in μm for 1C03 probe: influence of fouling at $V \approx 0.55$ m/s

Impact angles	"Clean" probe	Number of runs	"Dirty" probe	Number of runs
$\gamma \approx \beta \approx 0^\circ$	38.4	6	38.6	3
$\gamma \approx \beta \approx 30^\circ$	55.4	2	46.5	7

Even if the rise time is weakly modified by fouling, there is a basic difference between clean and dirty responses. In the latter case, the start of the ascending ramp is delayed compared to the former case. This has been confirmed by quasi-steady piercing experiments on probe 1C02; the delay can be very high, up to a few hundreds of micrometers, and diminishes as the probe is progressively cleaned. The example of Fig. 20 is intermediate; the delay is about 80 μm. This tendency is to be related to the time evolution of the liquid film which sticks to a dirty probe, and remains in place for some time before it is drained. Although additional work is needed on this problem, especially under dynamic conditions, the above tests have shown that the phase detection could be sensitive to fouling. In contrast, rise times, and thus velocity measurements, are nearly unaffected. This is confirmed by the coherency of the latency length measurements presented throughout this paper, for which no special care has been taken with probe cleanliness or liquid purity.

5. Conclusion

Cleaved, conical and cleaved–conical monofiber optical tips have been analysed with the prospect of obtaining the phase indicator function as well as inclusion velocities from the measurements of the duration of liquid-to-gas transitions. It is shown that a simulation of the optical phenomena based on geometrical optics, coupled with an idealised planar interface, illustrates the main features of actual probe responses. Notably, the origin of proximity detection has been explained, and the resulting error in gas residence time has been quantified. Sharp conical tips have proven to be efficient for phase detection and for phase velocity measurements; trends in the latency length modification with the probe geometry have been exhibited. However, since conical tips are very sensitive to geometrical defects at their tip, it is presently rather difficult to manufacture such probes free from pre-signals and ensuring a precise control of their latency length. Consequently, experimental calibration is unavoidable for any sharp conical tip. In order to ensure a better a priori control of the probe response during its manufacture, new shapes will be investigated in a companion paper.

Acknowledgements

The authors are grateful to the DER-EdF for support of this research under grant no EdF T34L01/2K6727/RNE402. They are also thankful to P. Benech, LEMO, Grenoble for insightful discussions about probe manufacture and optical modelling.

References

Abuaf, N., Jones, O., Zimmer, G., Leonhardt, W., Saha, P. 1978. BNL flashing experiments: test facility and measurement techniques. In: Transient Two-Phase Flows. (Proc. of the 2nd CSNI Specialists Meeting, 12–14 June 1978, Paris) 2. 715–743.

Billingham, J., King, A., 1995. The interaction of a moving fluid/fluid interface with a flat plate. J. Fluid Mech. 269, 325–351.

Cartellier, A., 1990. Optical probes for local void fraction measurements: characterisation of performance. Rev. Sci. Instrum. 61 (2), 874–886.

Cartellier, A., 1992. Simultaneous void fraction measurement, bubble velocity, and size estimate using a single optical probe in gas–liquid two-phase flows. Rev. Sci. Instrum. 63 (11), 5442–5453.
Cartellier, A., Achard, J.L., 1991. Local phase detection probes in fluid/fluid two-phase flows. Rev. Sci. Instrum. 62 (2), 279–303.
Cartellier, A., Barrau, E., 1998. Monofiber optical probes for gas detection and gas velocity measurements: optimised sensing tips (referred to as part II). Int. J. Multiphase Flows **24,** 1295–1315.
Conley, M., Zarobilla, C., Freal, J., 1986. Reflection type fiber-optic sensor. Proceedings of SPIE, vol. 718, Fiber Optics and Laser Sensors IV, 22–24 Sept., Cambridge, MA, pp. 237–243.
Cubizolles, G., 1996. Étude stéréologique de la topologie des écoulements diphasiques à haute pression. Doctorat de L'École Centrale de Lyon, Janvier.
Flaming, D., Brown, K., 1982. Micropipette puller design: form of the heating element and effects of filament width on tip length and diameter. J. Neurosci. Meth. 6, 91–102.
Frijlink, J., 1987. Physical aspect of gassed suspension reactors. PhD Delft University of Technology, The Netherlands.
Gouirand, J.M., 1990. Technology and signal treatment development of optical probes for two-phase flow measurements. In: Proc. Optical Science and Engineering Congress, The Hague, The Netherlands 12–15 March.
Kent, F., Dudley, W., 1974. Optical properties of water in the near infrared. JOSA 64 (8), 1107–1110.
Machane, R., 1996. private communication.
Machane, R., Canot, E., 1995. Émergence de corps à la surface libre d'un fluide non-visqueux. Actes du12éme Cong. Français de Mécanique, 4–8 Sept., Strasbourg, pp. 165–169.
Miller, N., Mitchie, R., 1970. Measurement of local voidage in liquid/gas two phase flow systems using an universal probe. J. Brit. Nucl. Energy Soc. 2, 94–100.
Morris, D., Teyssedou, A., Lapierre, J., Tapucu, A., 1987. Optical fiber probe to measure local void fraction profiles. Appl. Opt. 26 (21), 4660–4664.
Okoshi, T., 1982. Optical Fibers. Academic Press, London.
Pinguet, B., 1994. Étude de sondes d'impédance pour la caractérisation d'écoulements diphasiques liquide–liquide en conduite inlinée. Doctorate de l'Univ. Pierre et Marie Curie, 16 Déc., Paris.
Podokorytov, D., Timkin, L., Chinnov, Y.E., 1989. A fiber-optics method for investigating boiling in cryogenic fluids. Soviet J. Appl. Phys. 3 (3), 136–144.
Quéré, D., 1991. Sur la vitesse minimale d'étalement forcé en mouillage partiel. C.R. Acad. Sci. Paris 313 (II), 313–318.
Royston, D., Waynant, R., Banks, A., Ramee, S., White, C., 1989. Optical properties of fiber optics surgical tips. Appl. Opt. 28 (4), 799–803.
Russo, V., Righini, G., Sottini, S., Trigari, S., 1984. Lens-ended fibers for medical applications; a new fabrication technique. Appl. Opt. 23 (19), 3277–3283.
Schmitt, A., Hoffmann, K., Loth, R., 1995. A transputer-based measuring system for decentralized signal processing applied to two-phase flow. Rev. Sci. Instrum. 66 (10), 5045–5049.
Sekoguchi, K., Takeishi, M., Kano, H., Hironaga, K., Nishiura, T., 1984. Measurements of velocity and void fraction in gas–liquid two-phase flow with an optical fiber. In: Proc. 2nd Int. Symp. on Applications of Laser Anemometry to Fluid Mechanics. paper 16.1, July 2–5, Lisbon.
Sene, K., 1984. Aspects of bubbly two-phase flow. Ph.D. Trinity College, Cambridge University, U.K.
Takahashi, K., 1990. Meniscus shape on small diameter fibers. J. Colloid Interface Sci. 134 (1), 181–187.
Vince, M., Breed, H., Krycuk, G., Lahey, R.T., Jr, 1982. Optical probe for high-temperature local void fraction determination. Appl. Opt. 21 (5), 886–892.
Werther, J., Molerus, O., 1973. The local structure of gas fluidized beds—I. A statistically based measuring system. Int. J. Multiphase Flow 1, 103–122.
Zun, I., Filipic, B., Perpar, M., Bombac, A., 1995. Phase discrimination in void fraction measurements via genetic algorithms. Rev. Sci. Instrum. 66 (10), 5055–5064.